energies

MDPI

Article

Impact of the KKL Correlation Model on the Activation of Thermal Energy for the Hybrid Nanofluid (GO+ZnO+Water) Flow through Permeable Vertically Rotating Surface

Doaa Rizk [1], Asad Ullah [2,*], Ikramullah [3], Samia Elattar [4,*], Khalid Abdulkhaliq M. Alharbi [5], Mohammad Sohail [6], Rajwali Khan [6], Alamzeb Khan [7] and Nabil Mlaiki [8]

1 Department of Mathematics, College of Science and Arts, Qassim University, Al-Asyah 52571, Saudi Arabia; d.hussien@qu.edu.sa
2 Department of Mathematical Sciences, University of Lakki Marwat, Lakki Marwat 28420, Pakistan
3 Department of Physics, Kohat University of Science & Technology, Kohat 26000, Pakistan; ikramullah@kust.edu.pk
4 Department of Industrial & Systems Engineering, College of Engineering, Princess Nourah bint Abdulrahman University, P.O. Box 84428, Riyadh 11671, Saudi Arabia
5 Mechanical Engineering Department, College of Engineering, Umm Al-Qura University, Makkah 24382, Saudi Arabia; kamharbi@uqu.edu.sa
6 Department of Physics, University of Lakki Marwat, Lakki Marwat 28420, Pakistan; msohail@ulm.edu.pk (M.S.); rajwali@ulm.edu.pk (R.K.)
7 Department of Pediatrics, Yale School of Medicine, Yale University, New Haven, CT 06511, USA; Alamzeb.khan@yale.edu
8 Department of Mathematics and Sciences, Prince Sultan University, P.O. Box 66833, Riyadh 11586, Saudi Arabia; nmlaiki@psu.edu.sa
* Correspondence: asad@ulm.edu.pk (A.U.); SAElattar@pnu.edu.sa (S.E.)

Citation: Rizk, D.; Ullah, A.; Ikramullah; Elattar, S.; Alharbi, K.A.M.; Sohail, M.; Khan, R.; Khan, A.; Mlaiki, N. Impact of the KKL Correlation Model on the Activation of Thermal Energy for the Hybrid Nanofluid (GO+ZnO+Water) Flow through Permeable Vertically Rotating Surface. *Energies* **2022**, *15*, 2872. https://doi.org/10.3390/en15082872

Academic Editors: Ishak Bin Hashim, Hussein A. Z. AL-bonsrulah, Dhinakaran Veeman and Mogalahalli V. Reddy

Received: 9 March 2022
Accepted: 12 April 2022
Published: 14 April 2022

Abstract: The thermal energy transfer characteristics during hybrid nanofluid migration are studied in the presence of a variable magnetic field, heat source, and radiation. The flow is governed by the conservation laws of mass, momentum, and energy, whereas it is modeled by the coupled set of nonlinear partial differential equations (PDEs). Suitable similarity transformations are employed to convert the developed set of PDEs to a nonlinear system of coupled ordinary differential equations (ODEs). The simplified system of ODEs is solved by using the well-established analytical procedure of homotopy analysis method (HAM). The effects of varying the strength of the physical parameters on the thermal energy transfer during hybrid nanofluid motion between two plates in which one of the plate is porous, rotating, as well as stretching are investigated through tables and two-dimensional graphs. The porosity is modeled through the Koo–Kleinstreuer model (KKL) correlation. The analysis reveals that the skin friction and Nusselt number augment with the increasing strength of the magnetic field and nanomaterials' concentrations. The gradient in the fluid velocity has a dual dependence on the strength of the applied magnetic field and Grashof number and drops with the higher values of the unsteadiness parameter. The fluid velocity constricts with the enhancing magnetic field due to higher Lorentz forces, and it also drops with the increasing rotation rate. The enhancing buoyancy associated with higher Grashof number values augments the fluid velocity. The fluid's temperature rises with the augmenting nanomaterial concentrations, Eckert number, nonsteadiness, heat source strength, and radiation parameter, while it drops with the higher Grashof number and Prandtl number. The applied technique of the HAM shows good convergence over a wide range of the convergent parameter. This work has potential applications in the development of efficient thermal energy transfer systems.

Keywords: hybrid nanofluids; nonlinear thermal radiations; magnetic field; porous surface; HAM

1. Introduction

Thermal energy transfer has great importance and utilization in almost any type of physical process. Thermal energy transfer can take place due to conduction, convection, and radiation. The conduction involves the transfer of heat due to direct contact, whereas convection occurs due to the accumulative motion of the heated substance. Radiation is the mode of thermal energy transfer due to electromagnetic radiation. The ordinary fluids that are used for convective thermal energy transport are water, ethylene, ethylene glycol, etc. Due to low thermal conductivities, these ordinary fluids have limited thermal energy transfer efficiency. The thermal energy transport ability of ordinary liquids can be increased by adding solid particles of the appropriate size and nature. If the solid particles are in the nanometer size range and are metallic in nature, then their addition to ordinary fluids can increase the thermal energy transport efficiency enormously [1,2]. The fluid obtained due to the mixing of the ordinary fluid and nanoparticles is called a nanofluid. The idea of this fascinating fluid was developed by Choi [3] for the first time. The nanofluids are prepared by uniformly dispersing the nanomaterials in the ordinary liquids. The various thermophysical properties (for example, specific heat, thermal conductivity, and viscous nature) of such a type of fluid are highly dependent on the nanomaterial's associated characteristics, such as its nature, size, concentration, temperature, and the nature of the host fluid. Throughout the entire globe, researchers have studied the nanofluid thermal energy transfer efficiency under different constraints to model the nanofluid's behavior [4,5]. Nanofluid has been extensively employed in the storage of solar energy [6,7], thermal energy exchangers [8–10], freezing processes [11], thermal energy transport through radiations [12–14], etc. Mebarek-Oudina in [15] investigated the nanofluid thermal energy characteristics by using different base fluids. Muhammad et al. [16] simulated the nanofluid magneto-hydrodynamic (MHD) migration by incorporating the effects of the slip condition and motile microorganisms. Anum et al. [17,18] analyzed the sensitivity of different types of fluid numerically. The Darcy–Forchheimer nanofluid motion through a curved surface was analytically investigated by Sajjad et al. [19]. The nanofluid's mobility through an induced changing magnetic field by employing the second-grade fluid model was examined by Ambreen et al. [20]. Some recent investigations through computational and theoretical models to handle the heat exchange capabilities of nanofluids were performed in [21–23].

Recently, growing interest has developed in examining the thermal energy transport characteristics of hybrid nanofluids. Such types of fluids are obtained by intermixing nanomaterials of more than one type in the ordinary fluids. Hybrid nanofluids possess distinct and improved thermophysical characteristics as compared with the single-component nanofluid. There exists various kinds of hybrid nanoliquids [24–26]. The tremendous amount of research work displays that hybrid nanofluid are more versatile in comparison with the ordinary nanofluid. Suresh et al. [27] examined the thermal characteristics of a hybrid nanofluid consisting of copper and alumina nanoparticles using the two-step approach. Chamkha et al. [28] simulated the time-varying conjugate motion of the ($Cu+Al_2O_3+H_2O$) hybrid nanofluid through a triangular container. The authors reported a substantial enhancement in the Nusselt number. Momin [29] experimentally investigated the hybrid nanofluid mixed convective laminar flow through an inclined tube. The improved thermal energy transfer characteristics and the friction parameter of the ($MWCNT+Fe_3O_4+H_2O$) hybrid nanofluid were examined by Sundar et al. [30]. Ghachem et al. [31] investigated the rate of heat energy transfer through a heat exchanger employing the hybrid nanofluid. Lund et al. [32] studied the impact of viscous dissipation on the ($Cu+Al_2O_3+H_2O$) hybrid nanofluid's motion across squeezing surfaces using stability analysis. Suresh et al. [33] also investigated the possible merits of hybrid nano-powder (copper + alumina) for the efficient performance of a thermal energy system. They used water as the host fluid. Usman et al. [34] examined the hybrid nanofluid's ($Cu+Al_2O_3+H_2O$) motion from a permeable container taking into account the influences of varying thermal conduction and the source of nonlinear radiation suing LSM. The numerical examination of the impacts due to the ($MWCNT+Fe_3O_4+H_2O$) hybrid nanofluid's migration from a corrugated channel possessing separate heating/cooling sections was performed by Mohebbi et al. [35] employing the lattice Boltzmann method (LBM). Minna et al. [36] gave an overview by describing the hybrid nanofluids' development and their advantages.

This manuscript deals with the investigation of the thermal energy transfer characteristics of the hybrid nanofluid's (GO+ZnO+H_2O) migration between two plates in the presence of a varying magnetic field, radiation, and heat source. The right plate is porous, rotating with an angular velocity Ω and stretching with velocity u. This work has potential applications in the development of efficient thermal energy transfer systems using hybrid nanofluids. The structure of the present articles is as follows:

The hybrid nanofluid flow is modeled through coupled PDEs in Section 2. The coupled system of nonlinear PDEs is transformed to a simple form by using suitable similarity transformations in Section 3. The system of coupled ODEs is analytically solved using the HAM in Section 5. The results are obtained and then graphically displayed in Section 6. The work is then concluded in Section 7.

2. Mathematical Model of the Problem

The geometry of the studied problem is shown in Figure 1. It consists of two plates, in which the right plate rotates along the y-axis with angular velocity Ω and stretches along the x-axis with velocity u. The hybrid nanofluid (GO+ZnO+H_2O) is synthesized by mixing the nanoparticles of graphene oxide (Go) and zinc oxide (ZnO) with water (H_2O). The hydrothermal features of the hybrid nanofluid three-dimensional (3D), incompressible, and nonsteady motion are investigated in the presence of an applied variable magnetic field. The time dependence of the magnetic field is expressed by the relation $B(t) = B_0(1-\delta t)^{-0.5}$ and is acting along the y-axis. The temperature at the left wall is T_h and at the right wall is T_w. The gravitational force is acting vertically downward along the x-axis. We used the following assumptions in the current study:

- The flow is governed by the vessel wall with the stretching velocity $U_w = \chi x(1-\delta t)^{-1}$, where χ and δ are positive constants with $\delta t < 1$.
- The effective stretching rate $\chi(1-\delta t)^{-1}$ enhances subject to an external force acting along the $x-$axis for $0 \leq \delta < 1$.
- The Reynolds number (magnetic) is considered to be much less than unity to overcome the impact of the magnetic field induced.
- The magnetic field is applied in the transverse direction to the hybrid nanofluid flow.

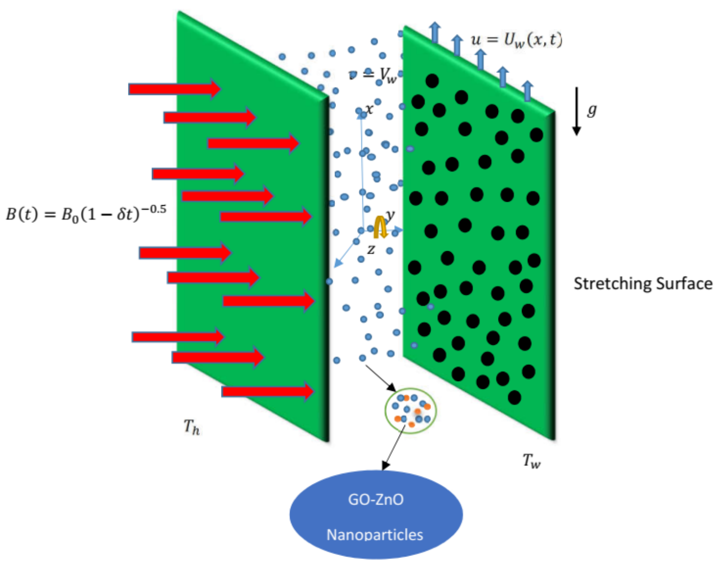

Figure 1. Geometrical display of the undertaken study.

The following equations model the hybrid nanofluid 3D flow: [37]:

$$u_x + v_y + w_z = 0, \tag{1}$$

$$\rho_{hnf}\Big(u_t + uu_x + vu_y + 2\Omega w\Big) = -p_x + \mu_{hnf}\Big(u_{xx} + u_{yy}\Big) - \sigma_{hnf}B^2(t)u + g(\rho\beta)_{hnf}\beta(T - T_w), \tag{2}$$

$$\rho_{hnf}\Big(v_t + uv_x + vv_y\Big) = -p_y + \mu_{hnf}\Big(v_{xx} + v_{yy}\Big), \tag{3}$$

$$\rho_{hnf}\Big(w_t + uw_x + vw_y - 2\Omega w\Big) = \mu_{hnf}\Big(w_{xx} + w_{yy}\Big) - \sigma_{hnf}B^2(t)w, \tag{4}$$

$$\begin{aligned}(\rho C_p)_{hnf}\Big(T_t + uT_x + vT_y + wT_z\Big) = k_{eff}\Big(T_{xx} + T_{yy+T_{zz}}\Big) + \mu_{hnf}\Big(2\Big[u_x^2 + v_y^2 + w_z^2\Big] + v_x^2 + v_z^2 + \\ \Big(w_x + u_z\Big)^2\Big) + Q_s(T - T_w) - q_y^r = 0,\end{aligned} \tag{5}$$

here, ρ_{hnf} (σ_{hnf}) is the hybrid nanofluid density (electrical conductivity), μ_{hnf} is the fluid dynamical viscosity, $B(t)$ is the applied time-varying magnetic field, Q_s is the heat generation/absorption rate, k_{hnf} is the thermal conductivity, and $(\rho C_p)_{hnf}$ is the specific heat at constant pressure. The flux (q_r) of radiation is expressed as [38]:

$$\frac{\partial q_r}{\partial y} = -\frac{16\sigma^s T_\infty^3}{3k_1}\frac{\partial^2 T}{\partial y^2}; \tag{6}$$

here, the symbol k_1 (σ^s) represents the average coefficient of absorption (Stefan–Boltzmann constant). The boundary conditions for Equations (1) to (5) are:

$$\begin{array}{lllll} u = U_w, & v = V_w, & w = 0, & T = T_h, & \text{at} \quad y = 0, \\ u \to 0, & v \to 0, & w \to 0, & T \to T_w, & \text{at} \quad y \to h. \end{array} \tag{7}$$

Here, $V_w = -\Big(\frac{\nu\chi}{1-\delta t}\Big)^{0.5} f(\eta)$ denotes the velocity of the water at the wall of the vessel at $\eta = 0$. Moreover, the slip factors for the state variables are ignored, and V_w corresponds to suction and injection subject to the cases $V_w < 0$ and $V_w > 0$, respectively. The hybrid nanofluid thermal expansion coefficient, thermal conductivity, electrical conductivity, specific heat, viscosity, and density are defined as follows:

$$\frac{(\rho\beta)_{hnf}}{(\rho\beta)_f} = (1 - \varphi_2)\Big[(1 - \varphi_1) + \varphi_1\Big(\frac{(\rho\beta)_{s1}}{(\rho\beta)_f}\Big)\Big] + \frac{\varphi_2(\rho\beta)_{s2}}{(\rho\beta)_f}, \tag{8}$$

$$\begin{aligned}\frac{k_{hnf}}{k_{bf}} &= (1 - \varphi_2) + 2\varphi_2\Big(\frac{k_{m2}}{k_{m2} - k_{bf}}\Big)ln\Big(\frac{k_{m2} + k_{bf}}{2k_{bf}}\Big), \\ \frac{k_{bf}}{k_f} &= (1 - \varphi_1) + 2\varphi_1\Big(\frac{k_{m1}}{k_{m1} - k_f}\Big)ln\Big(\frac{k_{m1} + k_f}{2k_f}\Big),\end{aligned} \tag{9}$$

$$\begin{aligned}\frac{\sigma_{hnf}}{\sigma_{bf}} &= \Bigg[1 + \frac{3\Big(\frac{\sigma_{m2}}{\sigma_{bf}} - 1\Big)\varphi_2}{\Big(\frac{\sigma_{m2}}{\sigma_{bf}} + 2\Big) - \Big(\frac{\sigma_{m2}}{\sigma_{bf}} - 1\Big)\varphi_2}\Bigg], \\ \frac{\sigma_{bf}}{\sigma_f} &= \Bigg[1 + \frac{3\Big(\frac{\sigma_{m1}}{\sigma_f} - 1\Big)\varphi_1}{\Big(\frac{\sigma_{m1}}{\sigma_f} + 2\Big) - \Big(\frac{\sigma_{m1}}{\sigma_f} - 1\Big)\varphi_1}\Bigg],\end{aligned} \tag{10}$$

$$\frac{(\rho C_p)_{hnf}}{(\rho C_p)_f} = \Big[(1 - \varphi_2)\Big(1 - \Big(1 - \frac{(\rho C_p)_{m1}}{(\rho C_p)_f}\Big)\varphi_1\Big) + \varphi_2\frac{(\rho C_p)_{m2}}{(\rho C_p)_f}\Big], \tag{11}$$

$$\frac{\mu_{hnf}}{\mu_f} = \frac{1}{(1-\varphi_1)^{2.5}(1-\varphi_2)^{2.5}}, \tag{12}$$

$$\frac{\rho_{hnf}}{\rho_f} = \left[(1-\varphi_2)\left(1-\left(1-\frac{\rho_{m1}}{\rho_f}\right)\varphi_1\right)+\varphi_2\frac{\rho_{m2}}{\rho_f}\right]. \tag{13}$$

The effective thermal conductivity is defined as follows:

$$k_{ef} = k_{sta} + k_{Brow}, \tag{14}$$

where, $k_{sta} = \left[(1-\varphi_2)+2\varphi_2\left(\frac{k_{m2}}{k_{m2}-k_{bf}}\right)ln\left(\frac{k_{m2}+k_{bf}}{2k_{bf}}\right)\right]\left[(1-\varphi_1)+2\varphi_1\left(\frac{k_{m1}}{k_{m1}-k_f}\right)ln\left(\frac{k_{m1}+k_f}{2k_f}\right)\right]$. Using the KKL correlation [39], k_{Brow} is given by:

$$k_{Brow} = 5\times 10^4\varphi(\rho C_p)_f\sqrt{\frac{k_bT}{\rho_p d_p}}f(\varphi,T), \tag{15}$$

where $k_{f,ef} = \frac{1}{R_f d_p + \frac{d_p^2}{K_f}}$ is widely used for k_f. Furthermore,

$$\begin{aligned} g'(\varphi,T,d_p) = &\Big(a_1 + a_2ln(d_p) + a_3ln(\varphi) + a_4ln(\varphi)ln(d_p) + a_5ln(d_p)^2\Big)ln(T) \\ &+\Big(a_6 + a_7ln(d_p) + a_8ln(\varphi) + a_9ln(\varphi)ln(d_p) + a_{10}ln(d_p)^2\Big), \end{aligned} \tag{16}$$

where the coefficients a_i for $i = 0,1,2,\ldots,10$ are used for the nanoparticles, and we have from Equation (15),

$$k_{Brow} = 5\times 10^4\varphi(\rho C_p)_f\sqrt{\frac{k_bT}{\rho_p d_p}}g'(\varphi,d_p,T). \tag{17}$$

On the other hand, the dynamic viscosity in functional form can be defined as:

$$\mu_{ef} = \mu_{sta} + \mu_{Brow} = \frac{k_{Brow}}{k_f}\times\frac{\mu_f}{Pr_f} + \mu_{sta}, \tag{18}$$

where $\mu_{sta} = \frac{\mu_f}{(1-\varphi_1)^{2.5}(1-\varphi_2)^{2.5}}$.

3. Similarity Transformations

The similarity transformations that are used to transform Equations (1)–(6) are expressed as [37]:

$$\begin{aligned} &u = \frac{\chi x}{(1-\delta t)}f'(\eta), v = -\left(\frac{\chi\nu}{1-\delta t}\right)^{0.5}f(\eta), \theta = \frac{T-T_w}{T_h-T_w}, \\ &w = -\left(\frac{\chi x}{1-\delta t}\right)^{0.5}g(\eta), \eta = y\left(\frac{\chi}{\nu(1-\delta t)}\right)^{0.5}. \end{aligned} \tag{19}$$

After applying the similarity transformations (19), we obtain:

$$f'''' - R\frac{\epsilon_1}{\epsilon_2}(f'f''' - ff'''') - 2Kr\frac{\epsilon_1}{\epsilon_2}g' - \epsilon_5\frac{M}{A_2}f'' - Re\frac{\epsilon_1}{\epsilon_2}Gr_m\beta^*\theta' - A_0(\frac{\eta}{2}f'' + f') = 0, \tag{20}$$

$$g'' - R\frac{\epsilon_1}{\epsilon_2}(f'g - fg') + 2Kr\frac{\epsilon_1}{\epsilon_2}f' - \epsilon_5\frac{M}{\epsilon_2}g + A_0(\frac{\eta}{2}g' + g) = 0, \tag{21}$$

$$\theta'' + Pr\frac{\epsilon_2\epsilon_3}{\epsilon_1\epsilon_4}\left[Re\frac{\epsilon_1}{\epsilon_2}f\theta' + Ec\frac{\epsilon_1}{\epsilon_3}(4f'^2 + g^2) + \frac{\epsilon_1}{\epsilon_2\epsilon_3}ReQ\theta\right]/(1 + \frac{4Rd}{3\epsilon_4}) - A_0\frac{\eta}{2}\theta' = 0, \tag{22}$$

and the boundary conditions become

$$f(\eta) = S, f'(\eta) = 1, \theta(\eta) = 1, g(\eta) = 0 : \eta = 0, f'(\eta) \to 0, f(\eta) \to 0, g(\eta) \to 0, //\theta(\eta) \to 0 : \eta \to 1. \tag{23}$$

Here, $\epsilon_1 = \frac{\rho_{hnf}}{\rho_f}$, $\epsilon_2 = \frac{\mu_{eff}}{\mu_f}$, $\epsilon_3 = \frac{(\rho C_P)_{hnf}}{(\rho C_p)_f}$, $\epsilon_4 = \frac{k_{eff}}{K_f}$, $\epsilon_5 = \frac{\sigma_{hnf}}{\sigma_f}$, and $A_0 = \frac{\delta}{\chi}$ are constants, $Gr_n = \frac{g\beta_f(T_h - T_w)}{\chi^2 x}$ is the Grashof number, $\beta = \frac{\beta_{hnf}}{\beta_f}$ is the thermal expansion coefficient, $Q = \frac{Q_0}{\chi(\rho C_p)_f}$ is the heat source/sink parameter, $M = \frac{\sigma_f B_0^2 h^2}{\rho_f \nu_f}$ is the magnetic parameter, $kr = \frac{\Omega h^2}{\nu_f}$ is the rotation parameter, $Pr = \frac{\mu(\rho C_p)_f}{\rho_f k_f}$ is the Prandtl number, $Ec = \frac{\rho_f a^2 h^2}{(\rho C_p)_f(\theta_w - \theta_h)}$ is the Eckert number, $Rd = \frac{16\sigma^s T_h^3}{3kk^s}$ is the radiation parameter, and $Re = \frac{\chi h^2}{\nu_f}$ is the Reynolds number.

4. Engineering Quantities of Interest and Their Calculation

The quantities of engineering interest are defined as:

$$C_{fx} = \frac{\tau_w}{0.5\rho_{hnf}(U_w)}, Nu_x = \frac{xq_x}{k_{hnf}(T_w - T_\infty)}, \tag{24}$$

and

$$C f_x Re^{1/2} = \frac{2(1-\varphi_2)^{-2.5}}{(1-\varphi_1)^{2.5}} f''(0), \frac{Nu_x}{Re_x^{1/2}} = -k_{hnf} k_f^{-1} \theta'(0). \tag{25}$$

The thermo-physical characteristics of of hybrid nanomaterials, the physical model for the computation of the hybrid nanofluid's different properties, and the calculation of the skin friction and Nusselt number are given in Tables 1–3.

Table 1. Thermo-physical properties of GO, ZnO, and H_2O [40].

Properties (Thermo-Physical)	**k** $\left(\frac{W}{m.K}\right)$	**æ** $\left(\frac{Kg}{m^3}\right)$	$\mathbf{c_p}$ $\left(\frac{J}{Kg.K}\right)$
GO	5000	3600	765
H_2O	0.613	997.1	4179
ZnO	25	5700	523

Table 2. Variations in the $C f_x Re_x^{0.5}$ values under the impact of different parameters.

M	$\varphi_1 - \varphi_2$	kr	Gr_n	Cf_x
0.2	0.01	0.3	0.1	1.24321
0.4				1.49334
0.6	0.03			1.58438
	0.06			1.67854
		0.5		1.79825
		0.7		1.98252
			0.3	1.82112
			0.5	1.64678

Table 2 shows the computation of the skin friction Cf_x with changing M, $\varphi_1 - \varphi_2$, kr, and Gr_n. It is clear that the skin friction augments with the rising values of all these parameters, except Gr_n. The skin friction first augments and then drops with the rising Gr_n.

Table 3. Variations in the $Nu_x Re_x^{-0.5}$ values under the impact of different parameters.

$\varphi_1 - \varphi_2$	M	Q	Rd	Ec	Pr	Nu_x
0.01	0.2	0.1	0.1	1	6.0	0.112530
0.03						0.223450
0.06	0.4					0.238790
	0.6					0.339988
		0.3				0.441230
		0.6				0.541537
			0.3			0.651980
			0.6			0.767098
				2		0.889043
				3		0.892081
					6.3	0.742980
					6.6	0.705678

The computation of the Nusselt number (Nu_x) with changing values of the parameters $\varphi_1 - \varphi_2, M, Q, Rd, Ec$, and Pr is displayed in Table 3. The table shows that the Nusselt number augments with the increasing values of all these parameters, except Pr. The Nusselt number first rises and then drops with the rising Pr values.

5. Solution by the HAM

For a solution of the system of Equations (20)–(22) together with the boundary conditions (23), we used the HAM. The basic idea and use of the HAM are explained in [41–43]. For the solution purpose, we used the following conditions:

$$\hat{f} = 1 - \exp(\eta), \hat{\theta} = \exp(-\eta), \hat{\phi} = \exp(\eta), \tag{26}$$

satisfying the operators:

$$L_{\hat{f}}(\hat{f}) = f''', L_{\hat{\theta}}(\hat{\theta}) = \theta', L_{\hat{\phi}}(\hat{\phi}) = \phi'. \tag{27}$$

6. Results and Discussion

This section explains the hydrothermal features of the assumed hybrid nanofluid 3D motion through rotatory plates in the presence of a varying applied magnetic field. The variations of the state variables with the parameters of practical importance are graphically depicted.

Figure 2 displays the variation of $f'(\eta)$ with increasing strength of unsteadiness parameter A_0. The values of A_0 were taken as $1.0, 1.5, 2.0, 2.5$. At fixed A_0, the velocity field gradient drops with enhancing η. The augmenting A_0 causes the profile of $f'(\eta)$ to drop. The drop rate enhances with the increasing η. The different curves become almost parallel at the highest η. Thus, the increasing unsteadiness during the hybrid nanofluid motion mitigates the velocity field gradient due to the increasing turbulence associated with higher values of A_0.

The dependence of $f'(\eta)$ on the magnetic field strength through M is shown in Figure 3. Dual behavior is observed in the $f'(\eta)$ profile with increasing M. It is observed that $f'(\eta)$ drops with increasing M up to about $\eta = 0.5$ (mid the boundary layer) and then enhances. Both rates (drop and rise) augment with the increasing M as is clear from the increasing separation between different curves in both regions. It is therefore concluded that the increasing strength of the magnetic parameter results in a uniform velocity distribution for smaller η (near the hot plate), whereas this makes the velocity distribution non-uniform at higher η values due to higher dynamic viscosity of the fluid.

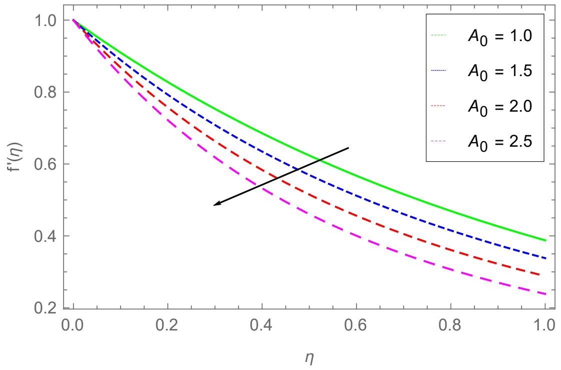

Figure 2. $f'(\eta)$ dependence on A_0.

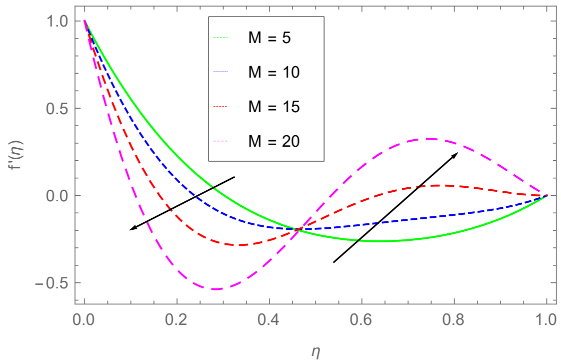

Figure 3. $f'(\eta)$ dependence on M.

The impact of enhancing magnetic field strength through the magnetic parameter (M) on the velocity $f(\eta)$ is displayed in Figure 4. The values of M were taken as $5.0, 10.0, 15.0, 20.0$. The graph shows that at fixed M, the velocity first enhances, attains the maximum value, and then, drops with the rising values of η. The augmenting M results in a drop in the $f(\eta)$ profile. The dropping rate enhances with the rising values of M as is clear from the increasing separation between different curves and is more drastic at the intermediate values of η. The various curves overlap at about $\eta = 0.9$. This drop in the fluid velocity is due to higher Lorentz forces, corresponding to higher values of M.

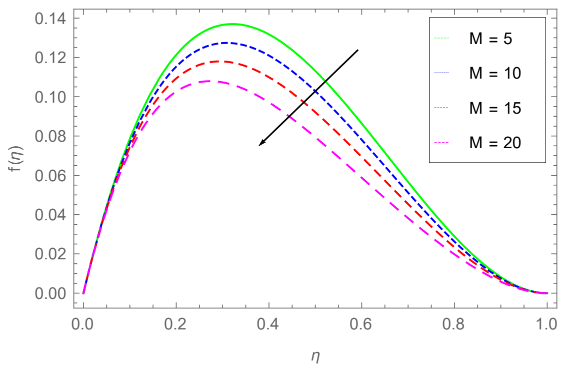

Figure 4. $f(\eta)$ dependence on M.

The variation of the fluid velocity $f(\eta)$ with enhancing Grashof number (Gr_n) is depicted in Figure 5. It is observed that for a given value of Gr_n, the fluid velocity first enhances, reaches the maximum, and then, drops to smaller values with the increasing η. The velocity profile rises with the augmenting Gr_n. The increase in the velocity profile is more prominent at the intermediate values of η as is clear from the wider separation between the different curves. The different curves overlap at about $\eta = 0.7$. Thus, the fluid presents a smaller opposing force to the flow due to lower viscosity at higher Gr_n values and, hence, augments the fluid velocity. This increase in velocity is appreciable only in the middle region of the boundary layer.

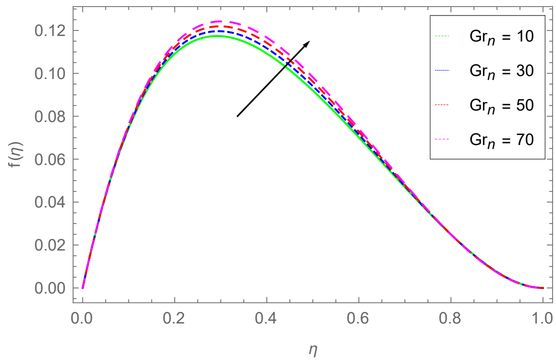

Figure 5. $f(\eta)$ dependence on Gr_n.

The impact of the enhancing Grashof number Gr_n on the velocity gradient $f'(\eta)$ is depicted in Figure 6. The values of Gr_n chosen were $10, 30, 50, 70$. The velocity gradient displays dual behavior with the augmenting Gr_n. At smaller η, the velocity gradient profile enhances, whereas at larger η, it drops with the increasing Gr_n. The figure also displays that the rate of drop is higher as compared to the rate of enhancement with the increasing Gr_n. Thus, the enhancing buoyancy associated with the higher values of Gr_n reduces the gradient in the fluid velocity beyond about the mid-point of the boundary layer. Therefore, it is concluded that the increasing buoyancy (decreasing viscosity) associated with higher Gr_n does not affect the velocity distribution of the hybrid nanofluid drastically.

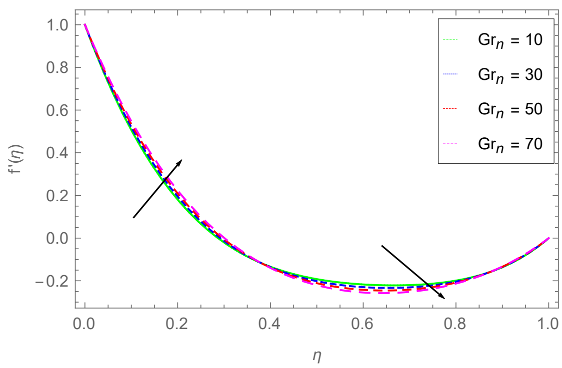

Figure 6. $f'(\eta)$ dependence on Gr.

The effect of enhancing values of the rotation parameter kr on the hybrid nanofluid velocity $f(\eta)$ is plotted in Figure 7. The values of kr were chosen as $1, 3, 5, 7$. Figure shows that at a given value of kr, the fluid velocity first enhances, reaches the maximum, and then, drops with the rising η. The figure also displays that the augmenting kr causes the fluid velocity profile to drop. The rate of velocity drop decreases with the increasing kr as displayed by the decreasing separation between the velocity curves at higher values of kr. The different curves overlap at about $\eta = 0.82$. Thus, the enhancing rotation rate offers a higher constriction to the fluid velocity, which causes the fluid velocity to drop. Thus, the enhancing rotation rate associated with the higher values of kr saturates the velocity drop during the hybrid nanofluid migration.

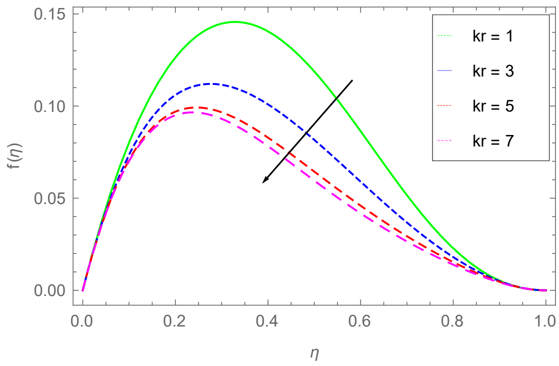

Figure 7. $f(\eta)$ dependence on kr.

Figure 8 depicts the dependence of $g(\eta)$ on the Grashof number Gr_n. It is evident that at a fixed value of Gr_n, the velocity component first increases, attains the maximum value, and then, drops to smaller values with augmenting η. The increasing Grashof number values result in an enhancement in the velocity of the hybrid nanofluid. The increase in the velocity is more prominent at the intermediate values of η. The different curves overlap at about $\eta = 0.78$. Thus, the increasing buoyancy augments the hybrid nanofluid velocity.

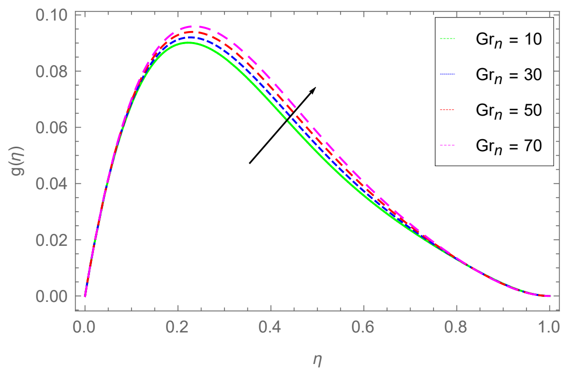

Figure 8. $g(\eta)$ dependence on Gr.

The impact of magnetic field strength through magnetic parameter M on the velocity component $g(\eta)$ is exhibited in Figure 9. The values of M were chosen as $5.0, 10.0, 15.0, 20.0$. The graph exhibits that the augmenting magnetic parameter strength drops the fluid velocity due to enhancing Lorentz forces acting on the fluid motion. Thus, the increasing magnetic parameter strength affects $g(\eta)$ drastically in the far region of the boundary layer due to the higher constriction of the flow in the comparatively colder region of the fluid.

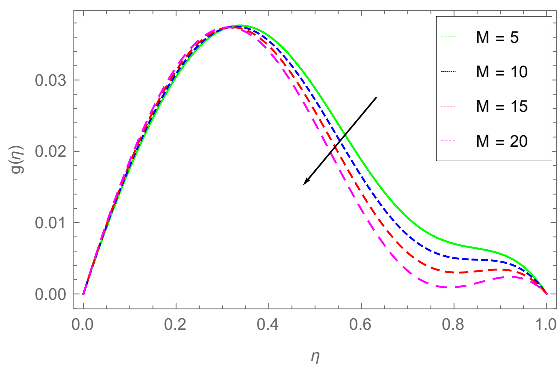

Figure 9. $g(\eta)$ dependence on M.

The variation of fluid's temperature $\theta(\eta)$ with a changing nanomaterials' concentration is depicted in Figure 10. The concentration of both types of nanomaterials was taken as equal. The figure displays that the enhancing fluid concentration causes the fluid's temperature to augment. The increase in fluid's temperature is more prominent with the increasing values of η, and this increase has almost the same rate for different values of the nanomaterials' concentrations as is clear from the equal spacing between different curves. It is also clear from the figure that at a fixed concentration, the fluid's temperature drops as we move away form the hot plate of the configuration.

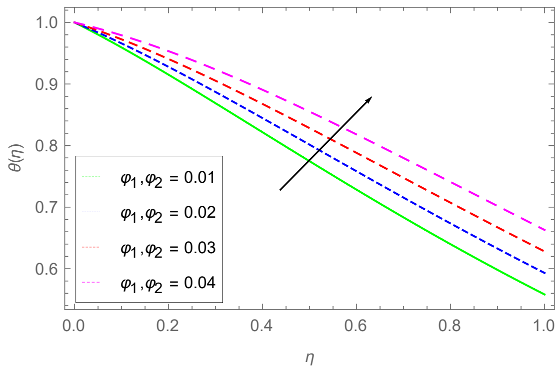

Figure 10. $\theta(\eta)$ dependence on nanomaterials' concentration φ_1,φ_2.

The variation of the fluid's temperature θ with enhancing values of the unsteadiness parameter A_0 is displayed in Figure 11. The figure shows that the increasing A_0 results in an enhancement in the fluid's temperature. The rate of enhancement with the rising A_0 remains almost constant as is clear from the equal separation between different curves. The different curves becomes almost parallel at the highest η. Furthermore, at fixed A_0, the fluid's temperature drops as we move away from the hot plate.

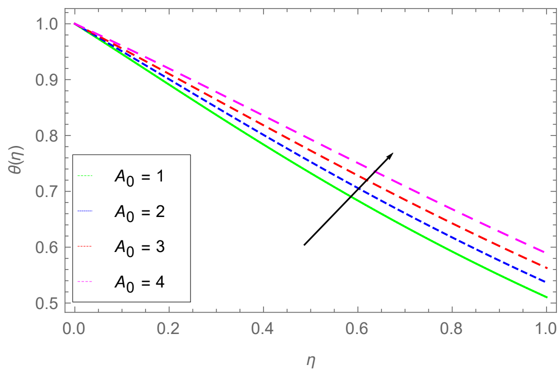

Figure 11. $\theta(\eta)$ dependence on A_0.

Figure 12 shows the variation of the temperature distribution with the enhancing Eckert number Ec. The values of Ec were taken as $1.0, 1.5, 2.0, 2.5$. It is evident from the figure that the rising Ec values augment the fluid's temperature. The rate of increase rises with the higher Ec values as evident from the wider separation between different curves. The different curves overlap at about 0.9. Thus, the enhancing fluid velocity associated with higher values of Ec results in an increase in the heat dissipation, which augments the fluid's temperature distribution.

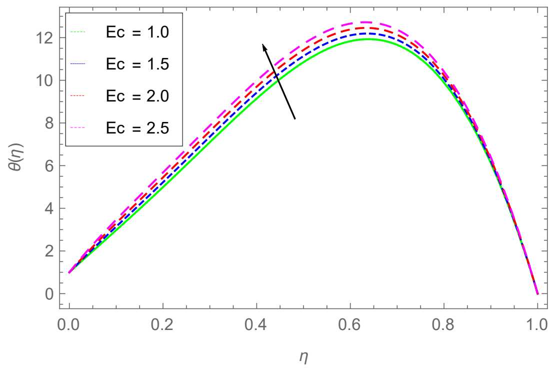

Figure 12. $\theta(\eta)$ dependence on Ec.

The dependence of the fluid's temperature on the enhancing values of the Grashof number Gr_n is plotted in Figure 13. The chosen values of Gr_n were $10, 30, 50, 70$. It is clear that the at given values of the Grashof number, the fluid's temperature first enhances, reaches the maximum, and then, drops with the rising values of the independent variable η. The augmenting strength of Gr_n reduces the fluid's temperature. The rate of the reduction of the fluid's temperature increases with the rising values of Gr_n as is clear from the greater separation between different curves. Furthermore, the dropping rate of the fluid's temperature is more drastic for the intermediate values of η. Thus, the decreasing viscous dissipation associated with the higher values of Gr_n reduces the fluid's temperature distribution.

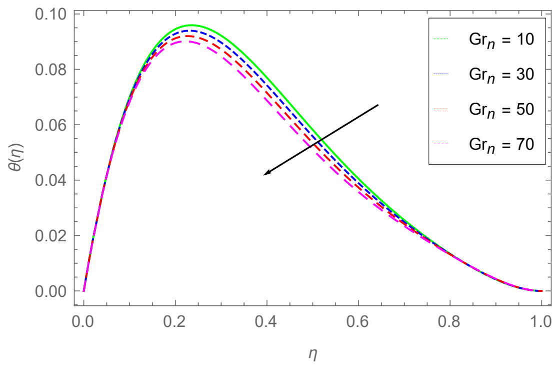

Figure 13. $\theta(\eta)$ dependence on Gr.

The impact of the enhancing Prandtl number Pr on the fluid's temperature distribution is displayed in Figure 14. The figure shows that the rising values of the Prandtl number result in a reduction in the fluid's temperature distribution. The rate of reduction of $\theta(\eta)$ is more prominent at the intermediate values of η. The different curves overlap at about $\eta = 0.9$. Thus, the increasing thermal diffusivity associated with the higher values of Pr reduces the fluid's temperature distribution, which is more prominent in the middle region of the system.

The impact of enhancing heat source strength Q on the fluid's temperature is displayed in Figure 15. The values of Q were chosen as $0.1, 0.2, 0.3, 0.4$. It is clear that the augmenting values of Q enhance the fluid's temperature distribution. The enhancement rate augments with the rising values of the source strength as evident from the larger separation between different curves. Furthermore, the enhancement rate is more obvious at the intermediate values of η.

The variation of the fluid's temperature with the rising strength of the radiation parameter Rd is exhibited in Figure 16. The graph shows that at a given value of Rd, the fluid's temperature drops with the rising η. The increasing values of Rd result in an enhancement in the fluid's temperature. The enhancement rate rises with the augmenting Rd values as evident from the increasing separation between different curves.

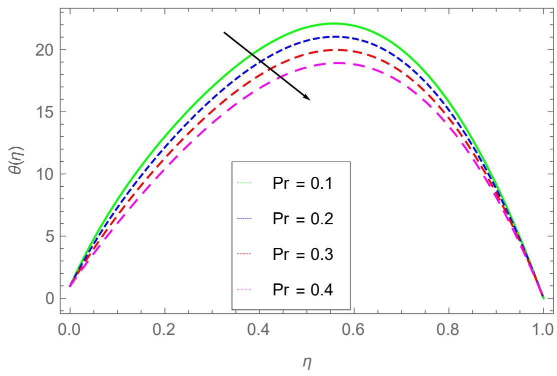

Figure 14. $\theta(\eta)$ dependence on Pr.

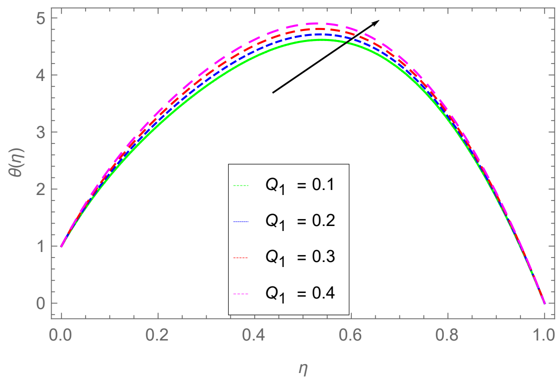

Figure 15. $\theta(\eta)$ dependence on Q.

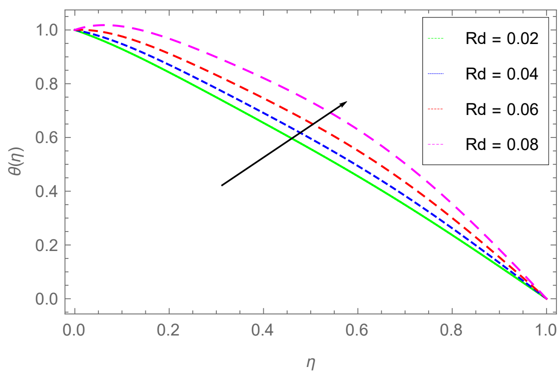

Figure 16. Impact of Rd on $\theta(\eta)$.

Convergence Analysis

The validity of the implemented technique for the transformed system of equations is based on the convergence of the series solution at $q = 1$, which is directly related to the h-curves. The suitable and educated guess of this parameter bounds the series to converge. Based on the assumptions and choice of certain parameters, Figure 17 displays the convergence analysis of the applied analytical procedure, the HAM. The figure shows that the HAM is convergent over a wide range of the convergent parameter h.

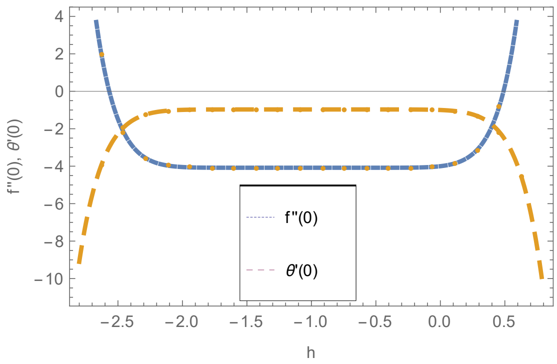

Figure 17. HAM's convergence.

7. Conclusions

The research work is concluded in this section. The heat transfer characteristics during the hybrid nanofluid's (GO+ZnO+H_2O) 3D incompressible unsteady motion between two parallel plates in the presence of an applied varying magnetic field were investigated. The right plate was porous, rotating with angular velocity Ω and stretching with velocity u. The flow was modeled using continuity, momentum, and energy equations. The system of developed coupled PDEs was transformed to a simple set of coupled ODEs through similarity transformations and then solved by employing the standard technique of the HAM. The impacts of the parameters of interest on the fluid motion were investigated through tables and graphs. The main findings of the current study are presented as follows:

- The skin friction augments with the rising magnetic parameter, the difference in nanomaterials' concentrations, and the rotation parameter.
- The Nusselt number rises with the enhancing magnetic field, heat source strength, radiation parameter, and Prandtl number.
- The gradient in the fluid velocity's horizontal component increases with the enhancing nonsteadiness parameter and has dual dependence on the augmenting magnetic field intensity.
- The horizontal component of the fluid velocity drops with the rising magnetic field and rotation parameter, whereas it rises with the increasing Grashof number.
- The vertical component of the fluid velocity rises with the increasing Grashof number and falls with the enhancing magnetic field strength.
- The hybrid nanofluid's temperature augments with the enhancing radiation parameter and the heat source strength, while it drops with the increasing Prandtl number, Grashof number, nonsteady parameter, and nanomaterials' concentrations.

Author Contributions: Conceptualization, S.E., A.U., M.S., A.K., and D.R.; software, D.R., R.K., A.U., K.A.M.A., S.E., and N.M.; writing—original draft preparation, I., R.K., M.S., A.K., and A.U.; writing—review and editing, D.R., S.E., R.K., I., and N.M.; formal analysis, M.S., K.A.M.A., I., and R.K.; validation, I., R.K., S.E., D.R., K.A.M.A., and A.U.; methodology, A.U., R.K., A.K., and M.S.; investigation, R.K., A.U., and I.; resources, D.R., A.U., S.E., and R.K.; project administration, A.U., A.K., M.S., and R.K.; funding acquisition, D.R. and S.E. All authors have read and agreed to the published version of the manuscript.

Funding: This research received no external funding.

Institutional Review Board Statement: Not applicable.

Informed Consent Statement: Not applicable.

Data Availability Statement: The data used to support the findings of this study are available within the article.

Acknowledgments: Princess Nourah bint Abdulrahman University Researchers Supporting Project number (PNURSP2022R163), Princess Nourah bint Abdulrahman University, Riyadh, Saudi Arabia.

The first author would like to thank the Deanship of Scientific Research, Qassim University, for funding the publication of this project. The authors would like to thank the Deanship of Scientific Research at Umm Al-Qura University for supporting this work by Grant Code: 22UQU4310392DSR05

Conflicts of Interest: The authors declare no conflict of interest.

References

1. Alsabery, A.; Chamkha, A.; Saleh, H.; Hashim, I. Natural convection flow of a nanofluid in an inclined square enclosure partially filled with a porous medium. *Sci. Rep.* **2017**, *7*, 2357. [CrossRef] [PubMed]
2. Xu, H.J.; Xing, Z.B.; Wang, F.; Cheng, Z. Review on heat conduction, heat convection, thermal radiation and phase change heat transfer of nanofluids in porous media: Fundamentals and applications. *Chem. Eng. Sci.* **2019**, *195*, 462–483. [CrossRef]
3. Choi, S.U.; Eastman, J.A. *Enhancing Thermal Conductivity of Fluids with Nanoparticles*; Technical Report; Argonne National Lab.: Argonne, IL, USA, 1995.
4. Al-Srayyih, B.M.; Gao, S.; Hussain, S.H. Effects of linearly heated left wall on natural convection within a superposed cavity filled with composite nanofluid-porous layers. *Adv. Powder Technol.* **2019**, *30*, 55–72. [CrossRef]
5. Mehryan, S.; Ghalambaz, M.; Izadi, M. Conjugate natural convection of nanofluids inside an enclosure filled by three layers of solid, porous medium and free nanofluid using Buongiorno's and local thermal non-equilibrium models. *J. Therm. Anal. Calorim.* **2019**, *135*, 1047–1067. [CrossRef]
6. Khanafer, K.; Vafai, K. A review on the applications of nanofluids in solar energy field. *Renew. Energy* **2018**, *123*, 398–406. [CrossRef]
7. Basha, H.T.; Sivaraj, R.; Reddy, A.S.; Chamkha, A. SWCNH/diamond-ethylene glycol nanofluid flow over a wedge, plate and stagnation point with induced magnetic field and nonlinear radiation–solar energy application. *Eur. Phys. J. Spec. Top.* **2019**, *228*, 2531–2551. [CrossRef]
8. Izadi, A.; Siavashi, M.; Xiong, Q. Impingement jet hydrogen, air and CuH_2O nanofluid cooling of a hot surface covered by porous media with non-uniform input jet velocity. *Int. J. Hydrogen Energy* **2019**, *44*, 15933–15948. [CrossRef]
9. Sabaghan, A.; Edalatpour, M.; Moghadam, M.C.; Roohi, E.; Niazmand, H. Nanofluid flow and heat transfer in a microchannel with longitudinal vortex generators: Two-phase numerical simulation. *Appl. Therm. Eng.* **2016**, *100*, 179–189. [CrossRef]
10. Ebrahimi, A.; Rikhtegar, F.; Sabaghan, A.; Roohi, E. Heat transfer and entropy generation in a microchannel with longitudinal vortex generators using nanofluids. *Energy* **2016**, *101*, 190–201. [CrossRef]
11. Siavashi, M.; Joibary, S.M.M. Numerical performance analysis of a counter-flow double-pipe heat exchanger with using nanofluid and both sides partly filled with porous media. *J. Therm. Anal. Calorim.* **2019**, *135*, 1595–1610. [CrossRef]
12. Ghadikolaei, S.; Hosseinzadeh, K.; Ganji, D.; Jafari, B. Nonlinear thermal radiation effect on magneto Casson nanofluid flow with Joule heating effect over an inclined porous stretching sheet. *Case Stud. Therm. Eng.* **2018**, *12*, 176–187. [CrossRef]
13. Kumar, M.A.; Reddy, Y.D.; Rao, V.S.; Goud, B.S. Thermal radiation impact on MHD heat transfer natural convective nano fluid flow over an impulsively started vertical plate. *Case Stud. Therm. Eng.* **2021**, *24*, 100826. [CrossRef]
14. Naranjani, B.; Roohi, E.; Ebrahimi, A. Thermal and hydraulic performance analysis of a heat sink with corrugated channels and nanofluids. *J. Therm. Anal. Calorim.* **2021**, *146*, 2549–2560. [CrossRef]
15. Mebarek-Oudina, F. Convective heat transfer of Titania nanofluids of different base fluids in cylindrical annulus with discrete heat source. *Heat Transf.—Asian Res.* **2019**, *48*, 135–147. [CrossRef]
16. Muhammad, T.; Alamri, S.Z.; Waqas, H.; Habib, D.; Ellahi, R. Bioconvection flow of magnetized Carreau nanofluid under the influence of slip over a wedge with motile microorganisms. *J. Therm. Anal. Calorim.* **2021**, *143*, 945–957. [CrossRef]
17. Shafiq, A.; Sindhu, T.N.; Khalique, C.M. Numerical investigation and sensitivity analysis on bioconvective tangent hyperbolic nanofluid flow towards stretching surface by response surface methodology. *Alex. Eng. J.* **2020**, *59*, 4533–4548. [CrossRef]
18. Shafiq, A.; Sindhu, T.N.; Al-Mdallal, Q.M. A sensitivity study on carbon nanotubes significance in Darcy—Forchheimer flow towards a rotating disk by response surface methodology. *Sci. Rep.* **2021**, *11*, 8812. [CrossRef]
19. Saif, R.S.; Hayat, T.; Ellahi, R.; Muhammad, T.; Alsaedi, A. Darcy—Forchheimer flow of nanofluid due to a curved stretching surface. *Int. J. Numer. Methods Heat Fluid Flow* **2019**, *29*, 2–20. [CrossRef]
20. Khan, A.A.; Naeem, S.; Ellahi, R.; Sait, S.M.; Vafai, K. Dufour and Soret effects on Darcy–Forchheimer flow of second-grade fluid with the variable magnetic field and thermal conductivity. *Int. J. Numer. Methods Heat Fluid Flow* **2020**, *30*, 4331–4347. [CrossRef]
21. Mahalakshmi, T.; Nithyadevi, N.; Oztop, H.F.; Abu-Hamdeh, N. MHD mixed convective heat transfer in a lid-driven enclosure filled with Ag-water nanofluid with center heater. *Int. J. Mech. Sci.* **2018**, *142*, 407–419. [CrossRef]
22. Sheikholeslami, M.; Rezaeianjouybari, B.; Darzi, M.; Shafee, A.; Li, Z.; Nguyen, T.K. Application of nano-refrigerant for boiling heat transfer enhancement employing an experimental study. *Int. J. Heat Mass Transf.* **2019**, *141*, 974–980. [CrossRef]
23. Zhang, L.; Bhatti, M.M.; Ellahi, R.; Michaelides, E.E. Oxytactic microorganisms and thermo-bioconvection nanofluid flow over a porous Riga plate with Darcy–Brinkman–Forchheimer medium. *J. Non-Equilib. Thermodyn.* **2020**, *45*, 257–268. [CrossRef]
24. Taylor-Pashow, K.M.; Della Rocca, J.; Huxford, R.C.; Lin, W. Hybrid nanomaterials for biomedical applications. *Chem. Commun.* **2010**, *46*, 5832–5849. [CrossRef]
25. Babazadeh, H.; Shah, Z.; Ullah, I.; Kumam, P.; Shafee, A. Analysis of hybrid nanofluid behavior within a porous cavity including Lorentz forces and radiation impacts. *J. Therm. Anal. Calorim.* **2021**, *143*, 1129–1137. [CrossRef]

26. Mehryan, S.; Izadpanahi, E.; Ghalambaz, M.; Chamkha, A. Mixed convection flow caused by an oscillating cylinder in a square cavity filled with Cu–Al_2O_3/water hybrid nanofluid. *J. Therm. Anal. Calorim.* **2019**, *137*, 965–982. [CrossRef]
27. Suresh, S.; Venkitaraj, K.; Selvakumar, P.; Chandrasekar, M. Synthesis of Al_2O_3–Cu/water hybrid nanofluids using two step method and its thermo physical properties. *Colloid Surf. A Physicochem. Eng. Asp.* **2011**, *388*, 41–48. [CrossRef]
28. Chamkha, A.J.; Miroshnichenko, I.V.; Sheremet, M.A. Numerical analysis of unsteady conjugate natural convection of hybrid water-based nanofluid in a semicircular cavity. *J. Therm. Sci. Eng. Appl.* **2017**, *9*, 041004. [CrossRef]
29. Momin, G.G. Experimental investigation of mixed convection with water-Al_2O_3 & hybrid nanofluid in inclined tube for laminar flow. *Int. J. Sci. Technol. Res* **2013**, *2*, 195–202.
30. Sundar, L.S.; Singh, M.K.; Sousa, A.C. Enhanced heat transfer and friction factor of MWCNT–Fe_3O_4/water hybrid nanofluids. *Int. Commun. Heat Mass Transf.* **2014**, *52*, 73–83. [CrossRef]
31. Ghachem, K.; Aich, W.; Kolsi, L. Computational analysis of hybrid nanofluid enhanced heat transfer in cross flow micro heat exchanger with rectangular wavy channels. *Case Stud. Therm. Eng.* **2021**, *24*, 100822. [CrossRef]
32. Lund, L.A.; Omar, Z.; Khan, I.; Seikh, A.H.; Sherif, E.S.M.; Nisar, K.S. Stability analysis and multiple solution of Cu–Al_2O_3/H_2O nanofluid contains hybrid nanomaterials over a shrinking surface in the presence of viscous dissipation. *J. Mater. Res. Technol.* **2020**, *9*, 421–432. [CrossRef]
33. Suresh, S.; Venkitaraj, K.; Selvakumar, P.; Chandrasekar, M. Effect of Al_2O_3–Cu/water hybrid nanofluid in heat transfer. *Exp. Therm. Fluid Sci.* **2012**, *38*, 54–60. [CrossRef]
34. Usman, M.; Hamid, M.; Zubair, T.; Haq, R.U.; Wang, W. Cu-Al_2O_3/Water hybrid nanofluid through a permeable surface in the presence of nonlinear radiation and variable thermal conductivity via LSM. *Int. J. Heat Mass Transf.* **2018**, *126*, 1347–1356. [CrossRef]
35. Mohebbi, R.; Izadi, M.; Delouei, A.A.; Sajjadi, H. Effect of MWCNT–Fe_3O_4/water hybrid nanofluid on the thermal performance of ribbed channel with apart sections of heating and cooling. *J. Therm. Anal. Calorim.* **2019**, *135*, 3029–3042. [CrossRef]
36. Minea, A.; Moldoveanu, M. Overview of hybrid nanofluids development and benefits. *J. Eng. Thermophys.* **2018**, *27*, 507–514. [CrossRef]
37. Sinha, A.; Misra, J.; Shit, G. Effect of heat transfer on unsteady MHD flow of blood in a permeable vessel in the presence of non-uniform heat source. *Alex. Eng. J.* **2016**, *55*, 2023–2033. [CrossRef]
38. Abdeljawad, T.; Ullah, A.; Alrabaiah, H.; Ayaz, M.; Khan, W.; Khan, I.; Khan, H.U. Thermal radiations and mass transfer analysis of the three-dimensional magnetite carreau fluid flow past a horizontal surface of paraboloid of revolution. *Processes* **2020**, *8*, 656. [CrossRef]
39. Ma, Y.; Mohebbi, R.; Rashidi, M.; Yang, Z. Koo–Kleinstreuer–Li correlation for simulation of nanofluid natural convection in hollow cavity in existence of magnetic field. *J. Therm. Anal. Calorim.* **2019**, *137*, 1413–1429. [CrossRef]
40. Goodarzi, M.; Toghraie, D.; Reiszadeh, M.; Afrand, M. Experimental evaluation of dynamic viscosity of ZnO–MWCNTs/engine oil hybrid nanolubricant based on changes in temperature and concentration. *J. Therm. Anal. Calorim.* **2019**, *136*, 513–525. [CrossRef]
41. Liao, S.J. The Proposed Homotopy Analysis Technique for the Solution of Nonlinear Problems. Ph.D. Thesis, Shanghai Jiao Tong University, Shanghai, China, 1992.
42. Liao, S. On the homotopy analysis method for nonlinear problems. *Appl. Math. Comput.* **2004**, *147*, 499–513. [CrossRef]
43. Liao, S. *Homotopy Analysis Method in Nonlinear Differential Equations*; Springer: Berlin/Heidelberg, Germany, 2012.